GFZ
Helmholtz-Zentrum
POTSDAM

Originally published as:

Lopez Comino, J. A., Cesca, S. (2018): Source complexity of an injection induced event: the 2016 Mw 5.1 Fairview, Oklahoma earthquake. - *Geophysical Research Letters*, *45*, 9, pp. 4025—4032.

DOI: http://doi.org/10.1029/2018GL077631

Geophysical Research Letters

RESEARCH LETTER
10.1029/2018GL077631

Key Points:
- Modeling the Mw 5.1 Fairview induced earthquake complex source by apparent source time functions and relative hypocenter-centroid location
- Identification of two sources, a mainshock and an early aftershock, favored by Coulomb stress changes
- Mainshock rupture directivity supports that the rupture growth is controlled by anthropogenic stress perturbation

Supporting Information:
- Supporting Information S1

Correspondence to:
J. A. López-Comino,
jalopez@gfz-potsdam.de

Citation:
López-Comino, J. A., & Cesca, S. (2018). Source complexity of an injection induced event: The 2016 M_w 5.1 Fairview, Oklahoma earthquake. *Geophysical Research Letters, 45*, 4025–4032. https://doi.org/10.1029/2018GL077631

Received 23 FEB 2018
Accepted 19 APR 2018
Accepted article online 30 APR 2018
Published online 15 MAY 2018

©2018. American Geophysical Union. All Rights Reserved.

Source Complexity of an Injection Induced Event: The 2016 M_w 5.1 Fairview, Oklahoma Earthquake

J. A. López-Comino[1] and **S. Cesca**[1]

[1]GFZ German Research Centre for Geosciences, Potsdam, Germany

Abstract Complex rupture processes are occasionally resolved for weak earthquakes and can reveal a dominant direction of the rupture propagation and the presence and geometry of main slip patches. Finding and characterizing such properties could be important for understanding the nucleation and growth of induced earthquakes. One of the largest earthquakes linked to wastewater injection, the 2016 M_w 5.1 Fairview, Oklahoma earthquake, is analyzed using empirical Green's function techniques to reveal its source complexity. Two subevents are clearly identified and located using a new approach based on relative hypocenter-centroid location. The first subevent has a magnitude of M_w 5.0 and shows the main rupture propagated toward the NE, in the direction of higher pore pressure perturbations due to wastewater injection. The second subevent appears as an early aftershock with lower magnitude, M_w 4.7. It is located SW of the mainshock in a region of increased Coulomb stress, where most aftershocks relocated.

Plain Language Summary Understanding the process of nucleation and rupture growth of natural and induced earthquakes is important for the assessment and mitigation of the corresponding time-dependent hazard. Advanced earthquake source analysis reveals significant properties such as rupture geometry, preferred direction of rupture propagation, and the configuration of main slip patches in an earthquake rupture. This work use the seismic recording of foreshocks and aftershocks to invert the source complexity of one of the largest earthquakes linked to wastewater injection, the 2016 M_w 5.1 Fairview, Oklahoma earthquake. Two subevents are clearly identified and their centroids are located with respect to the hypocenter. The first subevent has a magnitude of M_w 5.0 showing the main rupture propagated toward the NE, in the direction where the most of the wastewater injection activity is concentrated. The second subevent appears as an early aftershock with lower magnitude, M_w 4.7, located SW where most aftershocks were relocated. These results have important implications to discuss the role of anthropogenic stress perturbation in controlling the direction and extent of the earthquake rupture growth.

1. Introduction

Understanding the process of nucleation and rupture growth of natural and induced earthquakes is important for the assessment and mitigation of the corresponding time-dependent hazards to people and infrastructure. Extended or finite source inversions, including spatiotemporal tracking of the rupture evolution, provide important small-scale information on the complexity of the earthquake rupture process. For large, damaging earthquakes, there are still discrepancies on the resolution and robustness of these earthquake source inversions (e.g., López-Comino et al., 2015; Mai et al., 2016), making it challenging to extend such inversions to weak seismicity, for example, below moment magnitude M_w 5.5. Thanks to denser monitoring networks at local to regional scales, ongoing efforts in source characterization of weak to moderate earthquakes are continuing to actively address this challenge, allowing targeting of induced seismicity, which typically falls within this magnitude range (Atkinson et al., 2016; Lei et al., 2017; Yeck et al., 2017).

A detailed and robust analysis about the seismic source of suspected induced earthquakes helps to discriminate between natural, triggered, and induced earthquakes (Dahm et al., 2015). For example, early seismological work on the 2011 Prague (Oklahoma) earthquake sequence suggests a complex triggering process, with wastewater injection inducing a M_w 4.8 foreshock, which subsequently triggered the M_w 5.7 mainshock (Keranen et al., 2013). Posterior work focused on the modeling of the rupture process, using a finite-fault slip model; the relatively low peak slip and stress drop was interpreted to support the induced origin of the mainshock rupture (Sun & Hartzell, 2014). However, some cases remain debated, as the 2011 M_w 5.2 Lorca, Spain earthquake. Some authors correlated this event to groundwater exploitations (González et al., 2012), while others consider it a natural earthquake controlled by tectonic processes (López-Comino et al., 2012;

Morales et al., 2013). In this particular case, recent seismic source analysis revealed rupture directivity that could be inherent to the fault segment suggesting a natural seismic sequence (López-Comino et al., 2016).

Finite source inversions are challenging for weak to moderate events but require new approaches to robustly image small-scale source complexities. Generally, such seismic sources can at first order be modeled by circular or rectangular fault geometries, with symmetric or unilateral rupture propagation. The rupture size can be estimated using the magnitude and empirical relations (Wells & Coppersmith, 1994) or by determining rupture duration and assuming a realistic range of rupture velocities. Preferred directions of rupture propagation, so-called rupture directivity, have been described for weak earthquakes (e.g., Abercrombie et al., 2017; Kane et al., 2013; Lengliné & Got, 2011; Prieto et al., 2017). Apparent source time functions (ASTFs), robustly obtained from empirical Green's functions (EGFs) analysis, help to infer rupture directivity and complexity during the rupture growth (López-Comino et al., 2016; Stich et al., 2005). This work extends these techniques and allows one to resolve the source complexity of one of the largest earthquakes potentially linked to wastewater injection, the 2016 M_w 5.1 Fairview, Oklahoma earthquake. Yeck et al. (2016) first described this earthquake and the associated seismic sequence and suggested that the mainshock ruptured to the NE where the aftershocks delineated an aseismic region that may represent the major rupture area. Our analysis extends these results and expands our knowledge about the source complexities and implications.

2. Methods

2.1. ASTFs Analysis

Typically, the source complexity of small earthquakes (e.g., $M_w < 4.5$) in space and time can be neglected, and a point source approximation can be used. Their seismic recordings, referred as EGFs, can be used to accurately model the propagation effects between the source and receiver (Hartzell, 1978). This technique has been widely used for many years to investigate the complexity of larger events (mainshock) that share a similar hypocentral location and focal mechanism with the foreshock and/or aftershock used as an EGF (e.g., Baumont et al., 2002; López-Comino et al., 2012; Stich et al., 2007). The earthquake source for the mainshock can be isolated from seismograms through a deconvolution procedure between the mainshock and EGF waveforms, thus obtaining the ASTFs. ASTFs reveal the relative moment rate functions of the large event, as seen at each seismic station. In the presence of unilateral ruptures, smaller apparent durations identify the forward direction of the rupture directivity (Benioff, 1955; Ben-Menahem, 1961).

ASTF analysis is here performed for the M_w 5.1 Fairview earthquake using 16 foreshocks and aftershocks as EGFs (M_w between 4.4 and 3.4), having depths (±3 km) and faulting geometries (±13° for the strike of the preferred plane) similar to the ones found for the main event (Yeck et al., 2016). EGFs should typically be one to two magnitude units smaller than the mainshock, in order to represent an appropriate delta function. To obtain the ASTF, frequency domain deconvolution is performed through spectral division and is stabilized by a water level at 1% of the maximum spectral amplitude and a Gaussian low pass with pulse width of ~0.5 s (Figures S1 and S2 in the supporting information). We identify successful deconvolutions for *S* wave windows with length between 15 and 20 s. Stable ASTFs are observed for different EGFs revealing the source complexity of the target earthquake: Two source pulses slightly separated are easily identified at NE azimuths, while stations located toward SW record single pulses of overall shorter durations (Figure 1), which we interpret as the overlap of the two pulses observed at opposite azimuths. In order to homogenize the results, we select the M_w 3.9 aftershock on 2 March 2016 as the preferred EGF to obtain the ASTFs at all seismic stations. The selected EGF shows good-quality recording at all stations and is representative of the average ASTF from all EGFs. The azimuthal coverage is fairly complete using regional stations up to 570-km distance; however, the network is denser toward the east, where stations could be selected depending on their azimuth and data quality, than to the west (Figure 2a). ASTFs are normalized to unit area according to the total seismic moment of 4.98E + 16 Nm released for the M_w 5.1 Fairview earthquake. We removed negative values derived from the deconvolution procedure (Figure 2b). Apparent durations are estimated by manually picking the start time when energy in the observed window first becomes positive and the end time when positive amplitudes in the window cease. Note that for some stations this includes two separate pulses. The total duration error is estimated to be about 0.05 s. Resulting apparent durations range from 1.05 to 2.45 s (Figures 2a–2c). These durations exceed empirical values and durations resolved for M_w 5.1

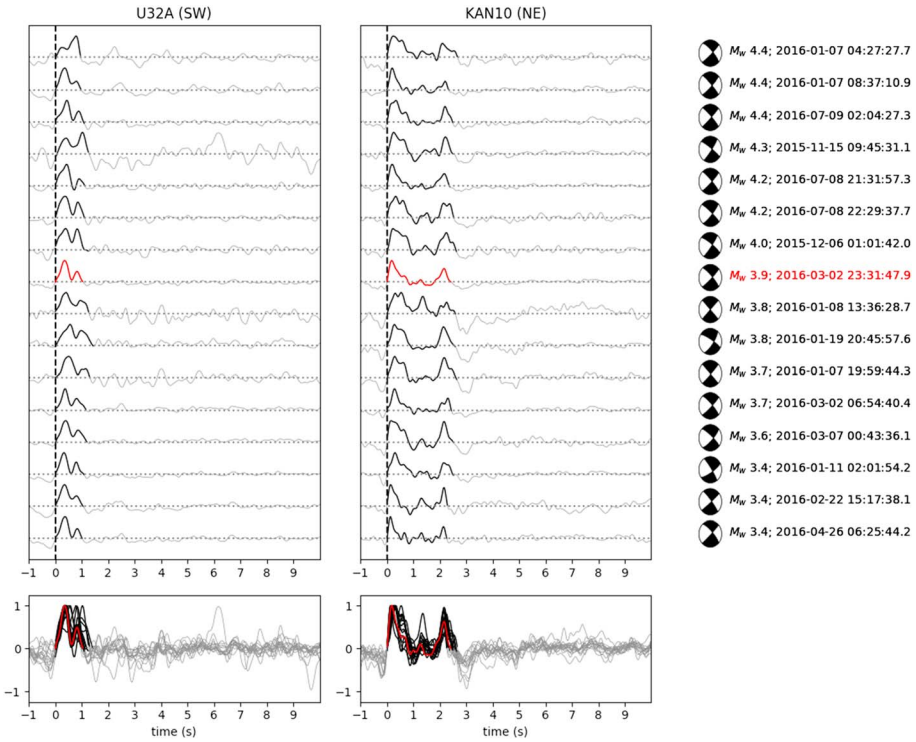

Figure 1. Apparent source time functions (ASTFs) for the 2016 M_w 5.1 Fairview, Oklahoma earthquake for two seismic stations (see Figure 2a) at SW direction, U32A (left) and NE direction, KAN10 (right), using different foreshock and aftershock as empirical Green's functions (EGFs). Each ASTF is labeled showing the corresponding moment tensor mechanism, moment magnitude, and origin time for each individual EGF, sorted in order of decreasing seismic moment (labels on right side). Lower panels show the overlapping of each ASTF for each seismic station normalized according to the maximum amplitude. Gray traces show the deconvolved functions from *S* waves through spectral division and the resulting ASTF is highlighted with a black line. Stable results using different EGFs are obtained, and we selected the M_w 3.9 aftershock on 2 March 2016 as a representative EGF from the solution (red traces).

earthquakes, which are typically about 1 s (López-Comino et al., 2016). This fact suggests that the ASTF complexity could be due to the presence of two subevents separated in space and time.

2.2. Relative Hypocenter-Centroid Location

A new approach is developed in order to infer the relative location for the two subevents identified from the ASTF analysis. The relative hypocenter-centroid location has been used in the past to distinguish among true and auxiliary planes of the focal mechanism (Zahradník et al., 2008). As for rupture directivity analysis, stations located in the direction of the second event, occurring later in time, show shorter apparent durations with overlapping pulses; in the opposite direction, we observe the maximum separation between the two subevents. We manually pick the beginning and end of each pulse associated to each subevent, whenever they are well separated, excluding those traces where these pulses overlap and their differential time cannot be accurately resolved (Figure 2b). The pulse represents the apparent moment rate function. The centroid time of each subevent, here referred as apparent centroid time (τ_{Ci}), is calculated as the time needed to release half of the scalar moment. The scalar moment ratio between the two subevents can also be estimated from the area defined below each pulse of the ASTFs, in order to quantify their magnitude and rupture size (Figure S3).

For a purely unilateral rupture, the azimuthal pattern of centroid apparent times as a function of azimuth for each subevent *i*, $\tau_{Ci}\,(\phi)$, can be written as

$$\tau_{\mathrm{Ci}}(\phi) = \Delta t_i - \frac{d_j \cos\delta}{v_{P,S}} \cos(\phi - \beta_i). \tag{1}$$

Variables in this model are the delay time between the centroid location of each subevent and the origin time, Δt_i; the distance from the centroid and the hypocenter location, d_j, where the index *j* indicates each

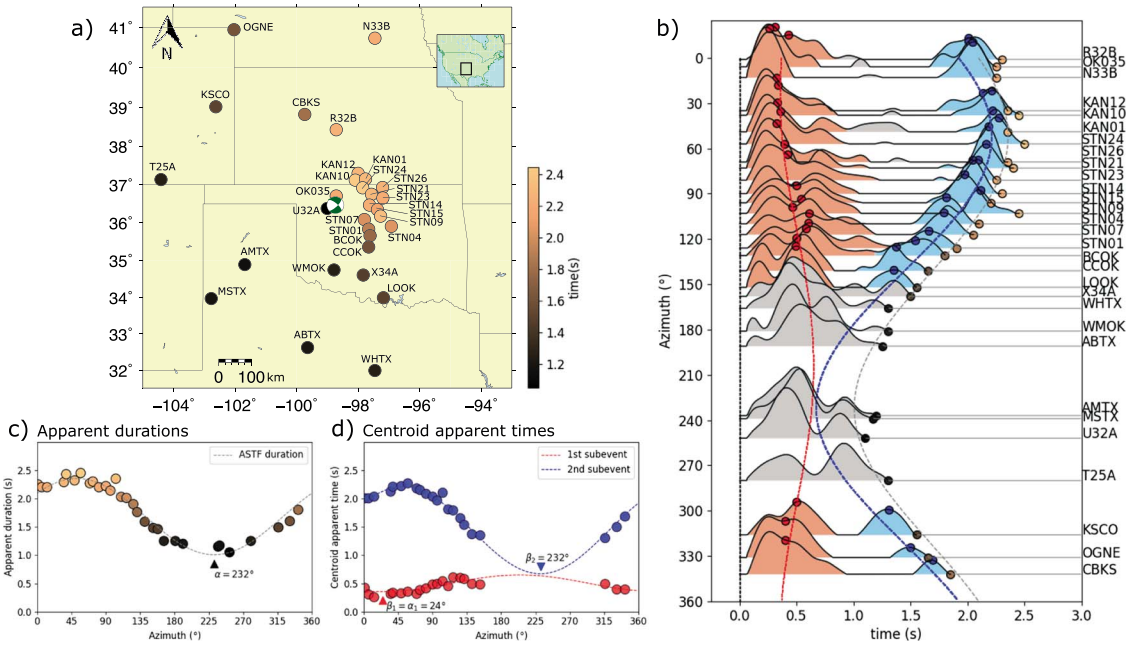

Figure 2. Apparent source time function (ASTF) analysis for the 2016 M_w 5.1 Fairview, Oklahoma earthquake. (a) Map of near-regional seismic stations used (circles) showing the apparent durations (color bar) and the moment tensor mechanism for the M_w 5.1 Fairview earthquake. (b) ASTFs for each seismic station identifying each pulse associated with the first subevent (red area) and second subevent (blue area), excluding the traces where these pulses are overlapped and the contribution for each subevent is not evident (gray area). Apparent durations (circles according the color bar in a) and centroid apparent times for each subevent (red and blue dots) are shown along the resulting models (gray, red, and blue dashed lines) from c and d. (c) Inversion of apparent durations for the M_w 5.1 Fairview earthquake using equation (2). Apparent durations identified in b (circles according to the color bar in a) along with the synthetic predictions for the inverted model (gray dashed lines) are shown. α indicates the predicted rupture directivity taking into account the apparent durations. (d) Inversion of centroid apparent times for each subevent using a full-grid search (equation (1)). Centroid apparent times from origin time identified in b for the first (red dots) and second (blue dots) subevent along with the synthetic predictions for the inverted model (red and blue dashed lines). β_1 and β_2 indicate the azimuth of the centroid for the first and second subevents; β_1 also represents the predicted rupture directivity for the first subevent (α_1).

grid point defined on the fault plane; and the azimuth of each subevent centroid with respect to hypocenter, β_i. We consider as fixed parameters P and S wave velocities, $v_{P,S}$ (depending on the wave type under consideration in the ASTF analysis) and the dip of the fault plane, δ. We assumed an S wave velocity of 3.5 km/s and dip of 70° according to previous work (Yeck et al., 2016). This equation is analogous to the parameterization of Cesca, Heimann, et al. (2011) for unilateral rupture where the apparent duration as a function of the azimuth $\tau\ (\phi)$ can be written as

$$\tau(\phi) = t_R - \frac{L_R}{v_{P,s}} \cos(\phi - \alpha) \tag{2}$$

but involving different variables: the rupture time (t_R), rupture length (L_R), and the azimuth of rupture directivity (α). The nonlinear inverse problem in equation (1) is solved through a full-grid search, and the model performance is evaluated through the L2 norm, obtaining a relative hypocenter-centroid location for each subevent, as well as its corresponding delay time (Figures 2d and 3). We note that β_1, describing the azimuth of the centroid for the first subevent, also represents the direction of rupture directivity, α_1.

3. Rupture Complexity of the M_w 5.1 Fairview Earthquake

ASTFs derived from the M_w 5.1 Fairview earthquake reveal a complex rupture, which may be linked to heterogeneous moment release involving either a complex rupture with two slip patches or two subevents. According to the parameterization of Cesca, Heimann, et al. (2011), the azimuthal pattern for the apparent durations is well adjusted for a unilateral rupture toward the SW (232° ± 5°), implying a total rupture time of 2.35 ± 0.05 s and a rupture length of 2.4 ± 0.2 km (Figure 2c). Parameter errors are approximated from the residuals using the Jacobian of partial derivatives of the function on each point as sensitivity matrix (López-Comino et al., 2016). These results reflect predominant rupture propagation coincident with the

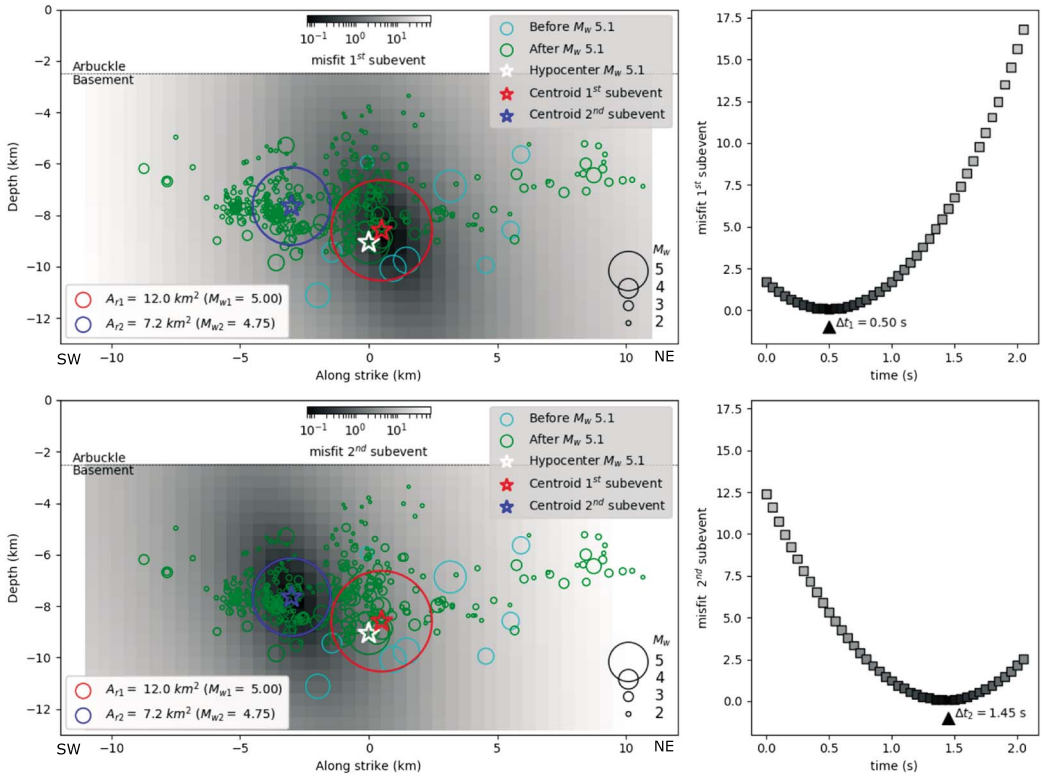

Figure 3. Relative hypocenter-centroid location for the first (top) and second (bottom) subevent. (left) a cross-sectional profile along the strike of the M_w 5.1 Fairview earthquake showing the misfit as a function of the centroid location for each subevent (the hypocenter location is denoted by a white star; the best centroid locations, by red and blue stars). Relocated earthquakes in the Fairview sequence are shown as open circles (Yeck et al., 2016), including earthquakes prior to the 13 February M_w 5.1 mainshock (cyan) and those after (green). Arbuckle-Precambrian interface (~2.5 km) is shown in dotted line (Campbell & Weber, 2006). Red and blue open circles indicate the estimated rupture area for each subevent. (right) Misfit for the delay time between the centroid location of each subevent and the origin time, Δt_i.

strike (~230°) of the main rupture plane but in the opposite direction suggested by previous work (Yeck et al., 2016). However, the total rupture time of this event appears inconsistent with empirical values for an earthquake with M_w ~ 5 as well as for estimated durations for other earthquakes of a comparable magnitude (López-Comino et al., 2016). Our interpretation, therefore, is that such long duration is the result of two subevents occurring with a small delay and separated by a small distance. The relative large separation between the two pulses (~0.8 s) observed in the ASTFs at NE azimuths strengthens our hypothesis to consider two subevents rather than a single mainshock. The complex *P* waveform of the mainshock, showing two subsequent pulses, can be also identified on selected displacement waveforms (Figure S4).

Consequently, we applied the proposed method to resolve the relative location between the hypocenter and the centroid of each subevent, through a full-grid search where the azimuthal pattern defined by the centroid apparent times are modeled (section 2.2). The fault plane is discretized into 45 × 23 sources with size of 0.5 × 0.5 km^2 covering an extended area defined by the relocated foreshock and aftershock according to the geometry described by Yeck et al. (2016). The centroid of the first subevent, which is more energetic, is located at ~0.51-km distance toward N24°E, with respect to the hypocenter. The second event occurs at much larger distance, at ~2.64 km in the opposite direction N232°E (Figures 2d and 3). The delay time between the origin time and each centroid time, tested for a reasonable interval between 0 and 2 s with increments of 0.05 s, is equal to 0.5 and 1.45 s (Figure 3), respectively. The relative moment ratio between the two subevents leads to an estimated magnitude of M_w 5.0 for the first subevent and M_w 4.7 for the second one. These magnitudes values suggest rupture areas of 12.0 and 7.2 km^2 for each subevent, according empirical relations for strike-slip earthquakes (Wells & Coppersmith, 1994) and assuming a circular rupture (Figure 3).

4. Discussion and Conclusions

Despite the weak magnitude of the Fairview earthquake, ASTF technique has allowed us to characterize successfully its rupture complexity. In our model, the mainshock is composed of two subevents. We develop and use a new approach to calculate the relative hypocenter-centroid location for each subevent through the modeling of centroid apparent times identified in the ASTFs. The first subevent, larger in magnitude, shows unilateral rupture propagation toward the NE. Its rupture area is located in proximity to an aseismic region delineated by the aftershocks (Yeck et al., 2016). The second subevent of lower magnitude affected a different region, toward the SW, at ~2.6-km distance from the hypocenter, where a second smaller aseismic region delineated by aftershocks can be observed (Figure 3). Even reducing by ~90° the azimuthal coverage due to pulse overlap (Figures 2b and 2d), remaining ASTFs can be used to robustly constrain rupture directivity of each subevent. We used a single EGF to recover ASTFs for two subevents, under the assumption that both subevents share a similar mechanism. This seems reasonable, considering the homogeneous mechanisms estimated for the whole aftershock sequence (Yeck et al., 2016 and Figure 1). The discovery that the M_w 5.1 mainshock is actually the combination of two subevents (mainshock and aftershock), with lower magnitudes M_w 5.0 and an M_w 4.7 is a key finding, with important implications for the assessment of maximum magnitudes for induced earthquakes (Galis et al., 2017; McGarr, 2014).

The basic mechanism of induced seismicity by industrial activities is well understood (Healy et al., 1968; Raleigh et al., 1976): The stress field of the shallow crust is altered by loading, mass shift, fluid injection, or reservoir depletion. The process of fluid injection may additionally increase the pore-fluid pressure and/or a change the state of stress, which may cause reactivation of existing faults or fractures. Fault rupture is often modeled by using the Mohr-Coulomb failure criterion (King et al., 1994) and the Coulomb stress gradient (ΔCFS), which is defined as the sum of the changes in the normal and shear stresses (Harris, 1998). In fluid injection operations the pressure of the fluids and the direction of pore pressure diffusion is well known, and thus the direction of ΔCFS can be estimated easily (Albano et al., 2017; Catalli et al., 2013; Deng et al., 2016).

Most of the injection activity is concentrated NE of the Fairview seismic sequence, at around 40-km distance, implying evidence for long-range poroelastic triggering derived from the fluid disposal wells (Goebel et al., 2017). Pore pressures and poroelastic stresses could have also played a role in controlling the rupture propagation and directivity of the first and largest subevent, which we resolved in the NE direction, toward the higher stressed region. According to Goebel et al. (2017), there is a clear gradient of pore pressure and poroelastic stresses, which at the Fairview site increases from SW to NE, toward the region with larger fluid injection operations. Assuming homogeneous friction conditions along the relatively small activated fault prior to the Fairview earthquake, we hypothesize that once the earthquake nucleates, the rupture more likely grows in accordance to such perturbed stress and pore pressure gradients. Some previous studies on injection induced earthquakes with similar magnitude have also resolved earthquake rupture propagating from low to high stress region (Dahm et al., 2007; Cesca, Dahm, et al., 2011). The second subevent appears as an early aftershock. As so, it is more likely to occur where the static stress increases and less likely where the stress decreases (King et al., 1994; Mallman & Parsons, 2008; Woessner et al., 2012). The SW relative location of the second subevent, in a region where most aftershocks were located, coincides with a positive Coulomb stress changes (Figure 3 in Yeck et al., 2016). This fact is supported by results in Yeck et al. (2016), where increases and decreases in ΔCFS agree with the observed aftershock locations. In conclusion, although the first subevent is controlled by anthropogenic stress perturbation supporting the results of Goebel et al. (2017), our interpretation suggests that the relative large distance (~40 km) of the Fairview sequence from the near-well regions of injection activity was not enough to control the rupture propagation of the second subevent and the following aftershock sequence, which are mainly affected by the local rupture process derived from the mainshock.

Rupture complexity of the Fairview earthquake involving a double event and rupture directivity effects in opposite directions evidences the challenging issue to determinate rupture directivity and discuss the factors that could control it. Treating the complex source as a single earthquake leads to the inference of SW rupture directivity, controlled by the moment releases of two subevents. However, our accurate source analysis separates the two events and further resolves the small-scale rupture directivity of the first event toward the NE. The knowledge about the initial properties as the spatial stress distribution before the earthquake rupture

could help to understand why unilateral or bilateral rupture modes are observed and why earthquake rupture propagates dominantly along a certain direction. For injection induced events, where pore pressure diffusion and stress perturbations can be modeled, appear as a favorable playground where the role of stress gradients on rupture growth can be tested.

Acknowledgments
This work is funded by the EU H2020 SHale gas Exploration and Exploitation induced Risks (SHEER) project (www.sheerproject.eu—grant agreement 640896). The authors would like to thank to Torsten Dahm and Arno Zang for comments and discussions. All waveform data used in this study are available at the IRIS DMC. The Fairview earthquake sequence catalog can be found at the supporting information by Yeck et al. (2016). Details on regional moment tensor solutions can be found at NEIC earthquake event pages and at http://www.eas.slu.edu/eqc/eqc_mt/MECH.NA/ (last accessed 2 February 2018).

References

Abercrombie, R. E., Poli, P., & Bannister, S. (2017). Earthquake directivity, orientation, and stress drop within the subducting plate at the Hikurangi margin, New Zealand. *Journal of Geophysical Research: Solid Earth*, *122*, 10,176–10,110. https://doi.org/10.1002/2017JB014935

Albano, M., Barba, S., Tarabusi, G., Saroli, M., & Stramondo, S. (2017). Discriminating between natural and anthropogenic earthquakes: Insights from the Emilia Romagna (Italy) 2012 seismic sequence. *Scientific Reports*, *7*, 282.

Atkinson, G. M., Eaton, D. W., Ghofrani, H., Walker, D., Cheadle, B., Schultz, R., et al. (2016). Hydraulic fracturing and seismicity in the western Canada Sedimentary Basin. *Seismological Research Letters*, *87*, 631–647. https://doi.org/10.1785/0220150263

Baumont, D., Courboulex, F., Scotti, O., Melis, N. S., & Stavrakakis, G. (2002). Slip distribution of the M_w 5.9, 1999 Athens earthquake inverted from regional seismological data. *Geophysical Research Letters*, *29*(15), 1720. https://doi.org/10.1029/2001GL014261

Benioff, H. (1955). Mechanism and strain characteristics of the white wolf fault as indicated by the aftershock sequence. *Calif. Div. Mines Bull.*, *171*, 199–202.

Ben-Menahem, A. (1961). Radiation of seismic surface-waves from finite moving sources. *Bulletin of the Seismological Society of America*, *51*(3), 401–435.

Campbell, J. A. & Weber, J. L. (2006). Wells drilled to basement in Oklahoma, Oklahoma Geological Survey. Retrieved from http://www.ou.edu/content/ogs/publications/specialpublications.html

Catalli, F., Meier, M. A., & Wiemer, S. (2013). The role of coulomb stress changes for injection-induced seismicity: The Basel enhanced geothermal system. *Geophysical Research Letters*, *40*, 72–77. https://doi.org/10.1029/2012GL054147

Cesca, S., Dahm, T., Juretzek, K., & Kühn, D. (2011). Rupture process of the 2001 May 7 *M*W 4.3 Ekofisk induced earthquake. *Geophysical Journal International*, *187*, 407–413. https://doi.org/10.1111/j.1365-246X.2011.05151.x

Cesca, S., Heimann, S., & Dahm, T. (2011). Rapid directivity detection by azimuthal amplitude spectra inversion. *Journal of Seismology*, *15*, 147–164.

Dahm, T., Cesca, S., Hainzl, S., Braun, T., & Krüger, F. (2015). Discrimination between induced, triggered, and natural earthquakes close to hydrocarbon reservoirs: A probabilistic approach based on the modeling of depletion-induced stress changes and seismological source parameters. *Journal of Geophysical Research: Solid Earth*, *120*, 2491–2509. https://doi.org/10.1002/2014JB011778

Dahm, T., Krüger, F., Stammler, K., Klinge, K., Kind, R., Wylegalla, K., & Grasso, J. R. (2007). The 2004 Mw 4.4 Rotenburg, Northern Germany, earthquake and its possible relationship with gas recovery. *Bulletin of the Seismological Society of America*, *97*(3), 691–704.

Deng, K., Liu, Y., & Harrington, R. M. (2016). Poroelastic stress triggering of the December 2013 Crooked Lake, Alberta, induced seismicity sequence. *Geophysical Research Letters*, *43*, 8482–8491. https://doi.org/10.1002/2016GL070421

Galis, M., Ampuero, J. P., Mai, P. M., & Cappa, F. (2017). Induced seismicity provides insight into why earthquake ruptures stop. *Science Advances*, *3*, eaap7528.

Goebel, T. H. W., Weingarten, M., Chen, X., Haffener, J., & Brodsky, E. E. (2017). The 2016 Mw5.1 Fairview, Oklahoma earthquakes: Evidence for long-range poroelastic triggering at >40 km from fluid disposal wells. *Earth and Planetary Science Letters*, *472*, 50–61. https://doi.org/10.1016/j.epsl.2017.05.011

González, P. J., Tiampo, K. F., Palano, M., Cannavo, F., & Fernandez, J. (2012). The 2011 Lorca earthquake slip distribution controlled by groundwater crustal unloading. *Nature Geoscience*, *5*(11), 821–825.

Harris, R. A. (1998). Introduction to special section: Stress triggers, stress shadows, and implications for seismic hazard. *Journal of Geophysical Research*, *103*, 24,347–24,358.

Hartzell, S. H. (1978). Earthquake aftershocks as Green's functions. *Geophysical Research Letters*, *5*, 1–4.

Healy, J., Rubey, W., Griggs, D., & Raleigh, C. (1968). The Denver earthquakes. *Science*, *161*, 1301–1310.

Kane, D. L., Shearer, P. M., Goertz-Allmann, B. P., & Vernon, F. L. (2013). Rupture directivity of small earthquakes at Parkfield. *Journal of Geophysical Research: Solid Earth*, *118*, 212–221. https://doi.org/10.1029/2012JB009675

Keranen, K. M., Savage, H. M., Abers, G. A., & Cochran, E. S. (2013). Potentially induced earthquakes in Oklahoma, USA: Links between wastewater injection and the 2011 mw 5.7 earthquake sequence. *Geology*, *41*, 699–702.

King, G. C. P., Stein, R. S., & Lin, J. (1994). Static stress changes and the triggering of earthquakes. *Bulletin of the Seismological Society of America*, *84*, 935–953.

Lei, X., Huang, D., Su, J., Jiang, J., Wang, X., Wang, H., et al. (2017). Fault reactivation and earthquakes with magnitudes of up to Mw4.7 induced by shale-gas hydraulic fracturing in Sichuan Basin, China. *Scientific Reports*, *7*, 7971.

Lengliné, O., & Got, J. L. (2011). Rupture directivity of microearthquake sequences near Parkfield, California. *Geophysical Research Letters*, *38*, L08310. https://doi.org/10.1029/2011GL047303

López-Comino, J. A., Mancilla, F., Morales, J., & Stich, D. (2012). Rupture directivity of the 2011, Mw 5.2 Lorca earthquake (Spain). *Geophysical Research Letters*, *39*, L03301. https://doi.org/10.1029/2011GL050498

López-Comino, J. A., Stich, D., Ferreira, A. M. G., & Morales, J. (2015). Extended fault inversion with random slipmaps: A resolution test for the 2012 Mw 7.6 Nicoya, Costa Rica earthquake. *Geophysical Journal International*, *202*, 77–93.

López-Comino, J. A., Stich, D., Morales, J., & Ferreira, A. M. G. (2016). Resolution of rupture directivity in weak events: 1-D versus 2-D source parameterizations for the 2011, M_w 4.6 and 5.2 Lorca earthquakes, Spain. *Journal of Geophysical Research: Solid Earth*, *121*, 6608–6626. https://doi.org/10.1002/2016JB013227

Mai, P. M., Schorlemmer, D., Page, M., Ampuero, J. P., Asano, K., Causse, M., et al. (2016). The earthquake source inversion validation (SIV) project. *Seismological Research Letters*, *87*(3), 690–708.

Mallman, E. P., & Parsons, T. (2008). A global search for stress shadows. *Journal of Geophysical Research*, *113*, B12304. https://doi.org/10.1029/2007JB005336

McGarr, A. (2014). Maximum magnitude earthquakes induced by fluid injection. *Journal of Geophysical Research: Solid Earth*, *119*, 1008–1019. https://doi.org/10.1002/2013JB010597

Morales, J., Cantavella, J. V., Mancilla, F. L., Lozano, L., Stich, D., Herraiz, E., et al. (2013). The 2011 Lorca seismic series: Temporal evolution, faulting parameters and hypocentral relocation. *Bulletin of Earthquake Engineering*, *12*(5), 1871–1888.

Prieto, G. A., Froment, B., Yu, C., Poli, P., & Abercrombie, R. (2017). Earthquake rupture below the brittle-ductile transition in continental lithospheric mantle. *Science Advances*, *3*, e1602642.

Raleigh, C., Healy, J., & Bredehoeft, J. (1976). An experiment in earthquake control at Rangely, Colorado. *Science*, *191*, 1230–1237.

Stich, D., Mancilla, F., Baumont, D., & Morales, J. (2005). Source analysis of the M_w 6.3 2004 Al Hoceima earthquake (Morocco) using regional apparent source time functions. *Journal of Geophysical Research*, *110*, B06306. https://doi.org/10.1029/2004JB003366

Stich, D., Mancilla, F., Pondrelli, S., & Morales, J. (2007). Source analysis of the February 12th 2007, M_w 6.0 Horseshoe earthquake: Implications for the 1755 Lisbon earthquake. *Geophysical Research Letters*, *34*, L12308. https://doi.org/10.1029/2007GL030012

Sun, X., & Hartzell, S. (2014). Finite-fault slip model of the 2011 M_w 5.6 Prague, Oklahoma earthquake from regional waveforms. *Geophysical Research Letters*, *41*, 4207–4213. https://doi.org/10.1002/2014GL060410

Wells, D., & Coppersmith, K. (1994). New empirical relationships among magnitude, rupture length, rupture width, rupture area, and surface displacement. *Bulletin of the Seismological*, *84*(4), 974–1002.

Woessner, J., Jónsson, S., Sudhaus, H., & Baumann, C. (2012). Reliability of coulomb stress changes inferred from correlated uncertainties of finite-fault source models. *Journal of Geophysical Research*, *117*, B07303. https://doi.org/10.1029/2011JB009121

Yeck, W. L., Hayes, G. P., McNamara, D. E., Rubinstein, J. L., Barnhart, W. D., Earle, P. S., & Benz, H. M. (2017). Oklahoma experiences largest earthquake during ongoing regional wastewater injection hazard mitigation efforts. *Geophysical Research Letters*, *44*, 711–717. https://doi.org/10.1002/2016GL071685

Yeck, W. L., Weingarten, M., Benz, H. M., Mcnamara, D. E., Bergman, E., Herrmann, R. B., et al. (2016). Far-field pressurization likely caused one of the largest injection induced earthquakes by reactivating a large pre-existing basement fault structure. *Geophysical Research Letters*, *43*, 10,198–10,110. https://doi.org/10.1002/2016GL070861

Zahradník, J., Gallovic, F., Sokos, E., Serpetsidaki, A., & Tselentis, G. A. (2008). Quick fault-plane identification by a geometrical method: Application to the M_w 6.2 Leonidio earthquake, 6 January 2008, Greece. *Seismological Research Letters*, *79*, 653–662.